ADVANCED FUNCTIONAL MATERIALS
www.afm-journal.de

Check for updates

Constructing a Thin Disordered Self-Protective Layer on the $LiNiO_2$ Primary Particles Against Oxygen Release

*Jinniu Chen, Yang Yang, Yushu Tang, Yifan Wang, Hang Li, Xianghui Xiao, Suning Wang, Mariyam Susana Dewi Darma, Martin Etter, Alexander Missyul, Akhil Tayal, Michael Knapp, Helmut Ehrenberg, Sylvio Indris, and Weibo Hua**

One of the major challenges facing the application of layered $LiNiO_2$ (LNO) cathode materials is the oxygen release upon electrochemical cycling. Here it is shown that tailoring the provided lithium content during synthesis process can create a disordered layered $Li_{1-x}Ni_{1+x}O_2$ phase at the primary particle surface. The disordered surface, which serves as a self-protective layer to alleviate the oxygen loss, possesses the same layered rhombohedral structure ($R\bar{3}m$) as the inner core of primary particles of the $Li_{1-x}Ni_{1+x}O_2$ ($x \approx 0$). With advanced synchrotron-based x-ray 3D imaging and spectroscopic techniques, a macroporous architecture within the agglomerates of LNO with ordered surface (LNO-OS) is revealed after only 40 cycles, concomitant with the reduction of nickel on the primary particle surface throughout the whole secondary particles. Such chemomechanical degradation accelerates the deterioration of LNO-OS cathodes. Comparably, there are only slight changes in the nickel valence state and interior architecture of LNO with a thin disordered surface layer (LNO-DS) after cycling, mainly arising from an improved robustness of the oxygen framework on the surface. More importantly, the disordered surface can suppress the detrimental H2 ⇌ H3 phase transition upon cycling compared to the ordered one.

1. Introduction

The rapid development of high-energy Li-ion batteries (LIBs) for electric vehicles (EVs) puts an ever-increasing demand for high-nickel-content layered cathode materials.[1–3] By increasing nickel content in $LiNi_xCo_yMn_{1-x-y}O_2$ (NCM), the capacity of Ni-rich layered cathodes can be enhanced from 160 mAh g^{-1} ($LiNi_{1/3}Co_{1/3}Mn_{1/3}O_2$, NCM333) to 200 mAh g^{-1} ($LiNi_{0.8}Co_{0.1}Mn_{0.1}O_2$, NCM811).[4–6] Accordingly, NCM811 is capable of delivering a competitive energy density of about 300 Wh kg^{-1} at the cell level and is therefore regarded as one of the most promising cathode materials for the state-of-the-art LIBs used in EVs.[6–9] Meanwhile, the battery research community has devoted tremendous effort in developing layered cathodes with even higher Ni contents,[10–12] e.g., $LiNi_{0.9}Co_{0.05}Al_{0.05}O_2$[13] and $LiNi_{0.95}Co_{0.025}Mn_{0.025}O_2$.[14] After the discovery of $LiNiO_2$ (LNO) in the 1990s, it is always regarded as a theoretical target for maximum capacity, especially in recent years.[15–18] Despite the desirable energy density, LNO inherently suffers from severe oxygen loss, fast capacity fade, and structure deterioration during electrochemical cycling, as compared with the lower-Ni-content NCM cathode materials.[19,20]

While the surface coating[21] and other surface treatments[22–24] were used to suppress the loss of oxygen, they were often restricted by the anisotropic stress and low ionic conductivity owing to the incoherent coating shell or complicated

J. Chen, S. Wang, W. Hua
School of Chemical Engineering and Technology
Xi'an Jiaotong University
Xi'an, Shaanxi 710049, China
E-mail: weibo.hua@xjtu.edu.cn

Y. Yang, X. Xiao
National Synchrotron Light Source II (NSLS-II)
Brookhaven National Laboratory
Upton, NY 11973, USA

The ORCID identification number(s) for the author(s) of this article can be found under https://doi.org/10.1002/adfm.202211515.

© 2022 The Authors. Advanced Functional Materials published by Wiley-VCH GmbH. This is an open access article under the terms of the Creative Commons Attribution License, which permits use, distribution and reproduction in any medium, provided the original work is properly cited.

DOI: 10.1002/adfm.202211515

Y. Tang
Institute of Nanotechnology (INT)
Karlsruhe Institute of Technology (KIT)
Hermann-von-Helmholtz-Platz 1
76344 Eggenstein-Leopoldshafen, Germany

Y. Wang, H. Li, S. Wang, M. S. D. Darma, M. Knapp, H. Ehrenberg, S. Indris, W. Hua
Institute for Applied Materials (IAM)
Karlsruhe Institute of Technology (KIT)
Hermann-von-Helmholtz-Platz 1
D-76344 Eggenstein-Leopoldshafen, Germany

M. Etter, A. Tayal
Deutsches Elektronen-Synchrotron (DESY)
Notkestr. 85, 22607 Hamburg, Germany

A. Missyul
CELLS-ALBA Synchrotron
Cerdanyola del Valles, Barcelona E-08290, Spain

 © 2022 The Authors. Advanced Functional Materials published by Wiley-VCH GmbH

16163028, 0, Downloaded from https://onlinelibrary.wiley.com/doi/10.1002/adfm.202211515 by Karlsruher Inst F. Technologie, Wiley Online Library on [18/12/2022]. See the Terms and Conditions (https://onlinelibrary.wiley.com/terms-and-conditions) on Wiley Online Library for rules of use; OA articles are governed by the applicable Creative Commons License

doping effects. Recently, the Li/Ni antisite defect-rich surface in layered Ni-rich cathode materials, so-called passivated surface layer, was demonstrated to stabilize the layered surface structure and improve the cycling capacity.[17,25] When Li/Ni antisite defects occur in the near-surface region of Ni-rich crystallites, strong 180° Ni—O—Ni super exchange along chains stabilizes the disordered surface layers (**Figure 1**a,b).[26] For instance, Pan's group[27] reported that Ni-rich $LiNi_{0.8}Co_{0.2}O_2$ with a disordered layered phase at the particle surface can be achieved by Ti-gradient doping, such a disordered surface layer is inherently stable in the cubic close-packed (ccp) oxygen lattice to prevent oxygen release of $LiNi_{0.8}Co_{0.2}O_2$ cathode during cycling. However, a clear picture of how does the Li/Ni cation exchange on the surface of primary particles (i.e., lattice-coherent disordered surface layer) affect the chemomechanical degradation of LNO agglomerates over cycling is still lacking.

Herein, we describe how a partially Li/Ni disordered layered $Li_{1-x}(Ni)_{1+x}O_2$ ($R\bar{3}m$) on the surface of LNO primary particles is formed and controlled by the offered Li content during high-temperature solid-state reaction.[28,29] The advanced synchrotron-based nano-resolution (pixel size at 21 nm) spectro-tomography techniques[2,30–33] were utilized to spatially resolve the morphological and chemical characteristics in three dimensions within the secondary particles of two kinds of LNO oxides, one with ordered surface (LNO-OS) and the other one with disordered surface (LNO-DS). A 3D macroporous architecture was reconstructed non-invasively in the LNO-OS after only 40 cycles at 0.1 C between 2.8 and 4.3 V. Additionally, a reduction of Ni^{3+} on the primary particle surface was also revealed, offering an in-depth understanding of the capacity fade issue at the particle level. Very importantly, the morphology and capacity can be basically maintained in the fatigued LNO-DS cathode. Furthermore, a quasi-solid solution reaction is discovered in the LNO-DS electrode during cycling, in sharp contrast to the LNO-OS electrode (showing the well-known multiple-phase transition mechanism). These findings demonstrate that control of surface cation disorder could be a viable path for mitigating the chemical and structural instability problems in LNO cathode materials.

2. Results and Discussion

Two layered LNO oxides with different surface structures were prepared by adjusting the provided Li content. LNO-OS was obtained by heating of a mixture of $Ni(OH)_2$ ($P\bar{3}m1$) and 3% excess of $LiOH \cdot H_2O$ at 700 °C for 12 h under O_2 atmosphere, while the LNO-DS was synthesized by the same procedure in which the Li/Ni ratio was reduced to 0.95:1, details of the preparation process are shown in the supplementary methods section. The layered structure of both LNO-OS and LNO-DS is confirmed by the XRD patterns in Figure S1 (Supporting Information). High-angle annular dark field – scanning transmission electron microscopy (HAADF-STEM) image of LNO-DS (Figure 1d) displays that a certain amount of Ni ion migrates to the Li plane at surface-near regions (≈2 nm), contributing to the formation of the partially disordered layered $Li_{1-x}Ni_{1+x}O_2$ ($R\bar{3}m$). While a clear lattice fringe with a d-spacing of 4.7(1) Å (Figure 1g) is detected in LNO-OS, which corresponds to the interplanar distance between adjacent Ni layers (i.e., the (003) plane of the ordered layered $LiNiO_2$ ($R\bar{3}m$). Note that Ni cations in the Li layer are almost invisible in the surface region of LNO-OS, proving a low degree of Li^+/Ni^{2+} cation exchange at the surface of the particles (i.e., $x \approx 0$ in $Li_{1-x}Ni_{1+x}O_2$). Previous studies[28,29] have shown that a first-order phase transition from a metastable disordered Ni-rich $Li_{1-x}(TM)_{1+x}O_2$ ($R\bar{3}m$, TM = transition metal) to an equilibrium $Li(TM)O_2$ phase takes place as lithium/oxygen is incorporated during high-temperature lithiation reaction. On the basis of a thermodynamic view of crystal growth, the thermodynamically stable phase tends to have lower surface energies and moves to the inner region of the crystallites.[34,35] Since the provided Li content is smaller than the Ni content (n_{Li}:n_{Ni} <1), the metastable disordered $Li_{1-x}Ni_{1+x}O_2$ phase would be spontaneously formed in the surface near area of LNO-DS at a high annealing temperature of 700 °C. To evaluate the cation mixing in the surface-near region of LNO-DS, HAADF-STEM simulations were performed based on layered $[Li_{1-m}Ni_m]_{3a}[Ni_{1-m}Li_m]_{3b}O_2$ ($R\bar{3}m$, Figure S2, Supporting Information) or $[Li_{1-n}Ni_n]_{3a}[Ni]_{3b}O_2$ ($R\bar{3}m$, Figure S3, Supporting Information). The degree of Li/Ni exchange (m) is ≈0.4 without considering the lithium deficiency for the surface region of LNO-DS (Figure 1e; Figure S4, Supporting Information), and the concentration of Ni ions in the Li layer (n) is ≈0.7 without taking the Li/Ni exchange into account. Thus, the maximum value of x in the partially disordered layered $Li_{1-x}Ni_{1+x}O_2$ ($R\bar{3}m$) is supposed to be roughly equal to 0.7.

Electron energy loss spectroscopy (EELS) combined with STEM were used to identify the oxidation state information of LNO-DS at atomic resolution. The Ni L-edge chemical shift mapping of the selected region is exhibited in Figure 1j. The thin layer with a yellow color at the surface reveals a reduction of Ni ions. The spectra of Li K-edge/Ni M-edge, O K-edge, and Ni L-edge at the regions of interest (ROIs) marked in Figure 1j are provided in Figure 1k–m. To exclude the thickness effect of crystallites, the EEL spectra were normalized by the Ni M3-edge at ≈67 eV for comparing the relative intensities of Li K-edge. The reduction of the main Li K-edge peaks at ≈62 eV from ROI 3 to ROI 1 and 2 indicates a Li-poor area at the surface compared with the bulk of LNO-DS. The difference of the energy loss values at the highest point of pre-edge peak and main peak (ΔE) for the O K-edge at ROI 1, 2 and 3 are 10.9, 10.8, and 12.9, respectively. According to the literature,[36,37] the ΔE of partially disordered layered phase is located between 9.5 and 13.0, these two numbers are indicative of the fully disordered rock-salt-type phase ($Fm\bar{3}m$) and ordered layered phase ($R\bar{3}m$), respectively. Inspiringly, the presence of Li K-edge EEL spectra and the relatively high ΔE at the surface demonstrate that the Li-poor surface layer corresponds to the partially disordered layered $Li_{1-x}Ni_{1+x}O_2$ ($R\bar{3}m$) rather than the inactive NiO ($Fm\bar{3}m$) phase. The maximum of the Ni L_3-edge at the surface and in the bulk of LNO-DS occurs at 854 and 855 eV, respectively. Similar results can be found in other LNO-DS crystallites (Figure S5, Supporting Information), further proving a smaller Ni oxidation state (< +3) and a lower Li content in the near-surface region.

To acquire the average oxidation state and local environment of Ni ions, X-ray absorption spectroscopy (XAS) measurements in transmission mode were conducted on both, LNO-DS and

© 2022 The Authors. Advanced Functional Materials published by Wiley-VCH GmbH

16163028, 0, Downloaded from https://onlinelibrary.wiley.com/doi/10.1002/adfm.202211515 by Karlsruher Inst F. Technologie, Wiley Online Library on [18/12/2022]. See the Terms and Conditions (https://onlinelibrary.wiley.com/terms-and-conditions) on Wiley Online Library for rules of use; OA articles are governed by the applicable Creative Commons License

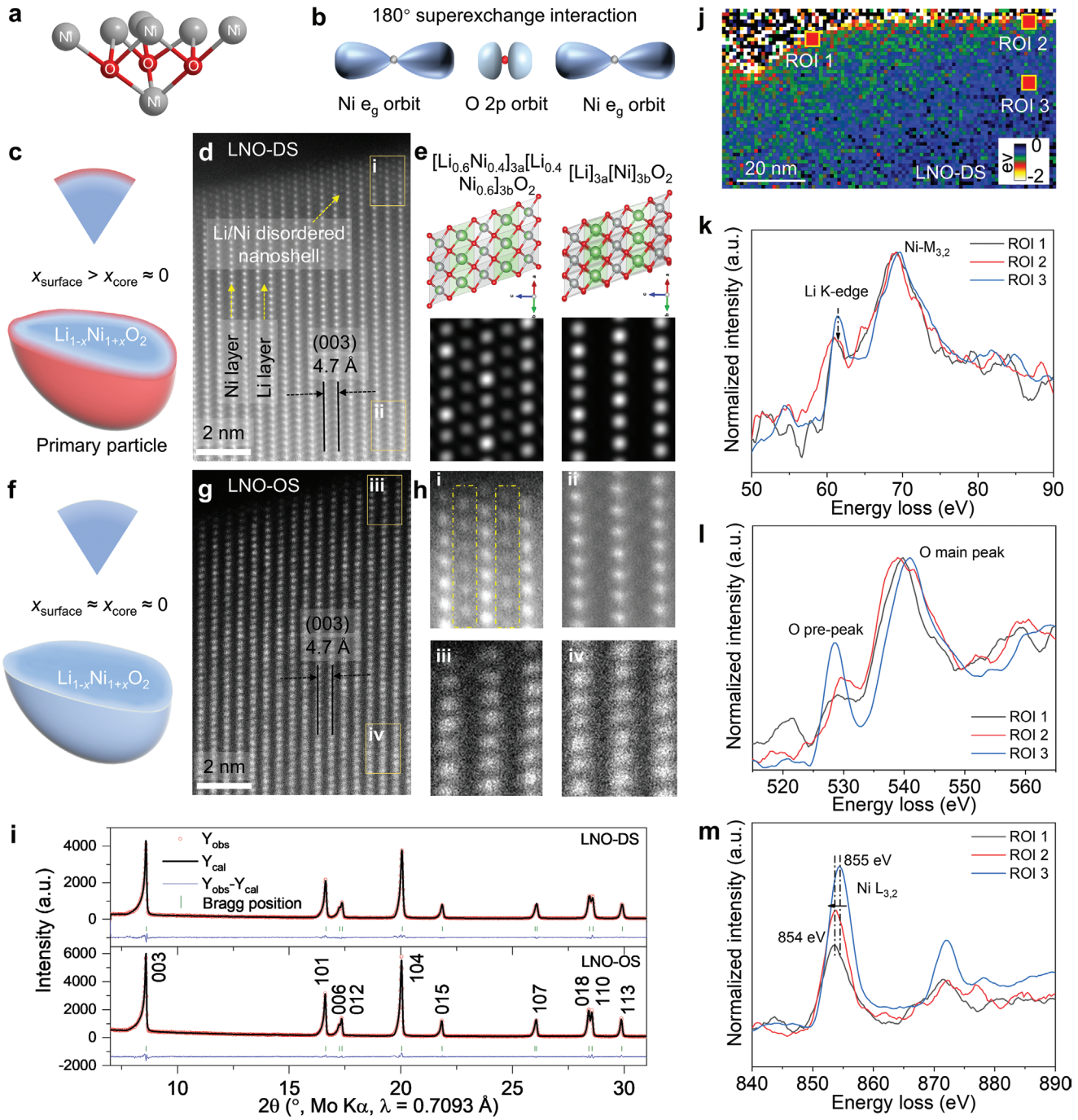

Figure 1. Comparison of the surface structures of LNO-DS and LNO-OS. a) Schematic illustration of linear super exchange interaction between three Ni in TM layer and one Ni in the Li layer. b) The orbital orientation of strong 180° super exchange interaction between O 2*p* orbital and Ni e_g orbital. Schematic of the cross-section of a $Li_{1-x}Ni_{1+x}O_2$ primary particle for c) LNO-DS and f) LNO-OS. The zoomed-in sector is a 2D cross-section from the particle surface to the bulk. The deeper blue color indicates lower Li/Ni disorder content, while the red color shows a higher degree of Li/Ni disorder. HAADF-STEM images of d) LNO-DS and g) LNO-OS from the surface to the inner area in a lattice-coherent particle. e) The structure models of the disordered layered $[Li_{0.6}Ni_{0.4}]_{3a}[Ni_{0.6}Li_{0.4}]_{3b}O_2$ ($R\bar{3}m$) and ordered layered $[Li]_{3a}[Ni]_{3b}O_2$ ($R\bar{3}m$), and the corresponding HAADF-STEM simulation images. h) Magnification of the region given in (d) and (g), rectangle i and iii are from the particle surface, rectangle ii and iv are from the bulk. The Ni pillars can clearly be seen in the Li layers in region i but not in other regions. i) Rietveld refinement against XRD patterns of LNO-DS (top) and LNO-OS (bottom). j) Ni L-edge chemical shift mapping, normalized EEL spectra of k) Li K-edge/Ni M-edge, l) O K-edge and m) Ni L-edge on surface and bulk of LNO-DS.

LNO-OS, compounds. There are no significant differences in the X-ray absorption near-edge structure (XANES) spectra of both materials (Figure S6a, Supporting Information), indicating that the average valence state of Ni is dominantly +3 for both oxides. The Fourier transform (FT *R*-space) magnitudes of extended x-ray absorption fine structure (EXAFS) spectra at Ni

 © 2022 The Authors. Advanced Functional Materials published by Wiley-VCH GmbH

16163028, 0, Downloaded from https://onlinelibrary.wiley.com/doi/10.1002/adfm.202211515 by Karlsruher Inst F. Technologie, Wiley Online Library on [18/12/2022]. See the Terms and Conditions (https://onlinelibrary.wiley.com/terms-and-conditions) on Wiley Online Library for rules of use; OA articles are governed by the applicable Creative Commons License

K-edge for two samples are plotted in Figure S6b (Supporting Information). There are almost no variations in the radial distribution function (RDF) peaks of both oxides, suggesting that the thin disordered surface dose not significantly affect the average local structure around Ni ions. The fitting results (Table S1, Supporting Information) confirm that the first and second peaks at about 1.5 and 2.5 Å arise from the Ni–O interactions with a bond distance of 2.0 Å and the Ni–Ni interactions with a bond distance of 2.9 Å, respectively. The relatively small values in peak maximum of the EXAFS RDF are because the FT R-profiles are not phase-corrected. All reflections in the XRD patterns of LNO-DS and LNO-OS can be indexed according to a layered rhombohedral phase with space group $R\bar{3}m$, see Figure 1i. Rietveld refinements were performed by using a layered structure model $[Li_{1-m}Ni_m]_{3a}[Ni_{1-m}Li_m]_{3b}O_2$ ($R\bar{3}m$). The residual weight percentages (R_{wp}) are about 5% for two samples, which suggests that the refinement results are believable. The obtained lattice parameters (e.g., a, c, and V) are listed in Tables S2 and S3 (Supporting Information), which are in good agreement with previously reported values of LNO.[15,38] The degree of Li/Ni mixing (m value) is as low as 0.02 for both oxides. No impurity phase is detected in the two samples. Generally, the Ni ions in the Li layer would generate 180° Ni–O–Ni super exchange chains in LNO oxides (see Figure 1a,b), where the oxygen anion between the spin parallel nickel creates σ-bonding with one nickel ion, and the oxygen anion between the spin antiparallel nickel produces π-bonding.[17,26] Such Li/Ni disordering on the surface is supposed to be beneficial for the improvement of the structural stability of LNO materials.[26,39]

The morphologies of LNO-DS and LNO-OS were studied by scanning electron microscopy (SEM), as shown in **Figure 2**a,c. Both samples compose of dense quasi-spherical-type secondary

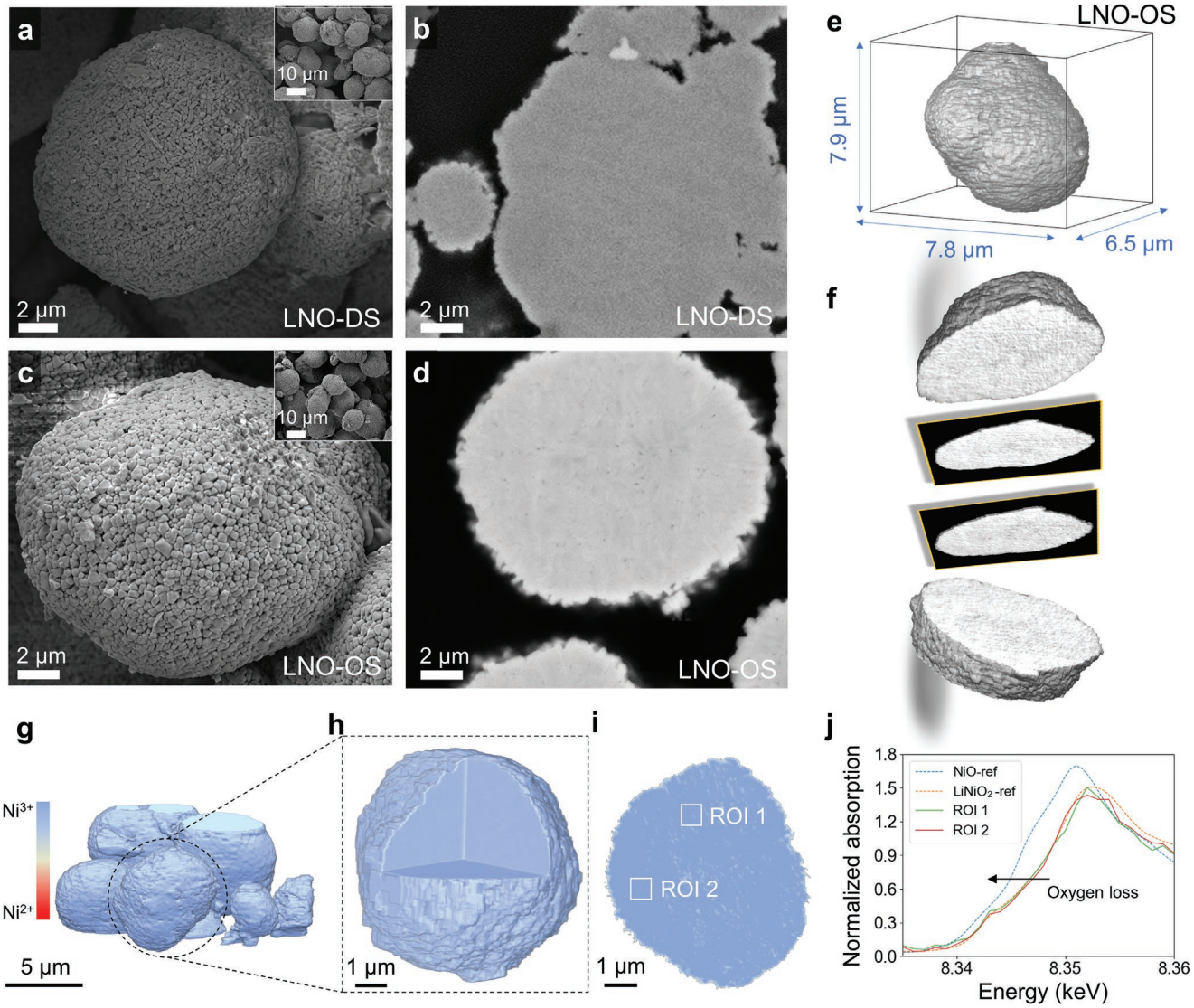

Figure 2. Spectro-microscopic investigation of pristine particles at multiple length scales. SEM images of a) LNO-DS and c) LNO-OS; cross-sectional SEM images of b) LNO-DS and d) LNO-OS; e) rendering of a particle of LNO-OS measured by 3D nano-tomography TXM, f) virtual internal view and the corresponding cross-sectional view of the selected particle; g) the over view and h) internal view of the 3D renderings of the Ni oxidation state distribution of LNO-OS; i) cross-sectional slides and j) the corresponding Ni K-edge XANES spectra over the regions of interest (ROIs) in (i).

© 2022 The Authors. Advanced Functional Materials published by Wiley-VCH GmbH

16163028, 0, Downloaded from https://onlinelibrary.wiley.com/doi/10.1002/adfm.202211515 by Karlsruher Inst F. Technologie, Wiley Online Library on [18/12/2022]. See the Terms and Conditions (https://onlinelibrary.wiley.com/terms-and-conditions) on Wiley Online Library for rules of use; OA articles are governed by the applicable Creative Commons License

particles with an average particle size of ≈8 µm. Each secondary particle is an agglomerate of small platelet-like primary nanosheets with a thickness of ≈60 nm and lateral dimensions ranging from 100 to 300 nm. Lens-based full-field transmission X-ray microscopy (synchrotron TXM) was further used to investigate the 3D internal architecture of compounds from nanometer to micrometer scales.[33] The geometry (shape and size) of a few randomly selected LNO-OS particles reconstructed from synchrotron TXM (Figure 2e; Figures S7–S13, Supporting Information) is consistent with SEM images. It can be observed from cross-sectional SEM and TXM images (Figure 2d,f) that the internal nanovoids (nanopores) are generated between primary particles. To obtain a depth profile of the Ni valence state, tomographic scans were conducted at a number of various energy levels across the absorption edge of Ni (8210–8700 eV). Correlating each pixel with energies in the Ni K-edge XANES spectra not only enables direct assessment of 2D/3D images, but also offers a relative probability distribution of Ni valence state by comparison with NiO and $LiNiO_2$ standards. XANES results (Figure 2j) illustrate that the valence state of Ni does not change significantly on the selected regions of LNO-OS particles, and remains +3, as evidenced by comparison with a $LiNiO_2$ standard sample. Uniform distribution of Ni^{3+} in the whole secondary particle is also clearly revealed by a homogenous light blue color distribution in Figure 2g–i.

The electrochemical performances of both LNO-DS and LNO-OS cathodes were evaluated by galvanostatic cycling of CR2032 coin-type half-cells under a C/10 rate (1 C = 280 mA g^{-1}) between 2.8 and 4.3 V at room temperature. The charge–discharge potential curves and the corresponding differential capacity as a function of voltage (dQ/dV vs V) profiles of selected cycles are presented in **Figure 3**a–d. For the first three formation cycles, the LNO-OS electrode delivers a high discharge capacity of ≈215 mAh g^{-1} (see Figure 3e). However, a severe capacity fading is pronouncedly observed in the LNO-OS cathode during extended cycling. Specifically, only ≈56% of its

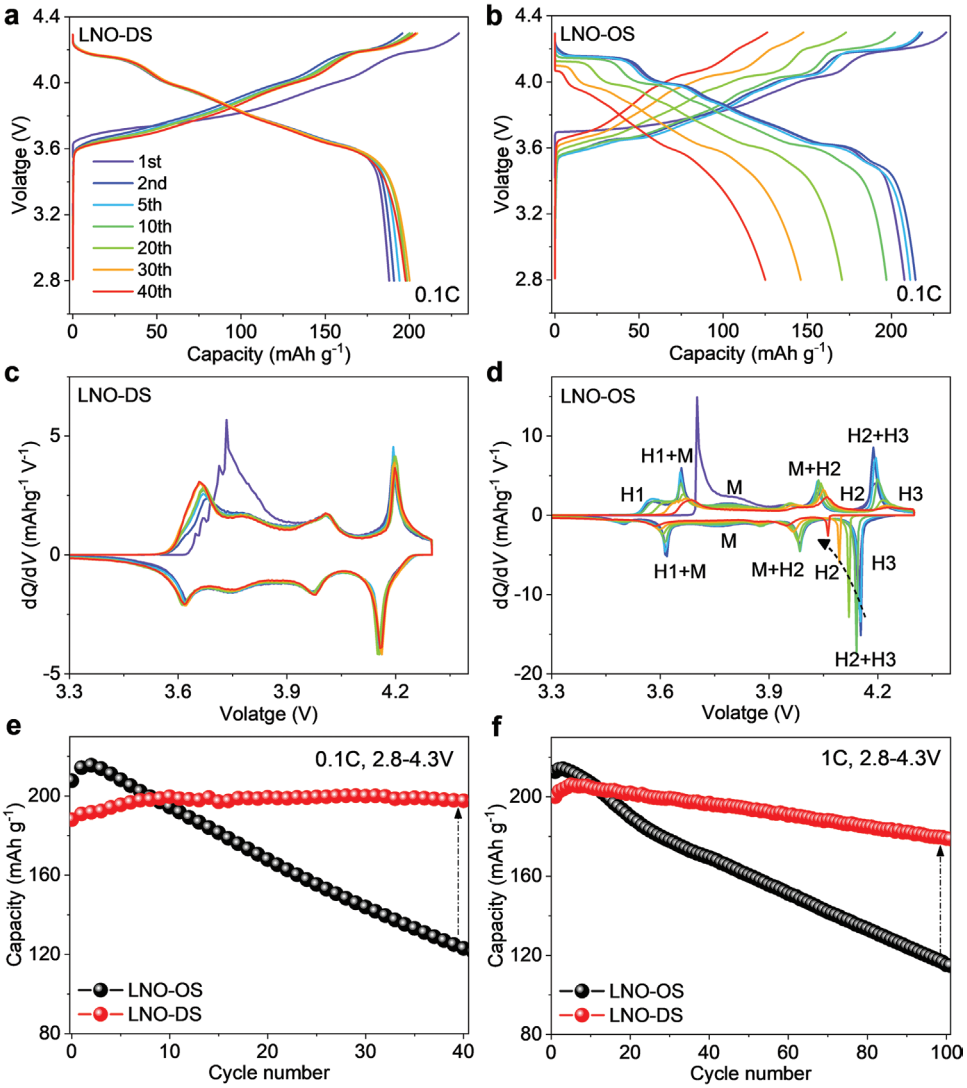

Figure 3. The electrochemical performance of two cathodes. The charge-discharge voltage profiles a) LNO-DS and b) LNO-OS cathodes from 1st to 40th cycle; the corresponding dQ/dV plots of c) LNO-DS and d) LNO-OS cathodes; the cyclability of two electrodes between 2.8 and 4.3 V at a current density of e) 0.1 C and f) 1 C.

© 2022 The Authors. Advanced Functional Materials published by Wiley-VCH GmbH

16163028, 0, Downloaded from https://onlinelibrary.wiley.com/doi/10.1002/adfm.202211515 by Karlsruher Inst F. Technologie, Wiley Online Library on [18/12/2022]. See the Terms and Conditions (https://onlinelibrary.wiley.com/terms-and-conditions) on Wiley Online Library for rules of use; OA articles are governed by the applicable Creative Commons License

initial capacity can be retained after 40 cycles. All peaks in the dQ/dV curves reflect the multiple phase transitions according to previous reports,[16,40] as described below for the in situ synchrotron-based X-ray diffraction (SXRD) results of the LNO-OS electrode. For the first charging, the H1 and H1+M peaks merge to one at higher potentials (≈3.7 V) because of the slow Li-ion transport at the beginning of de-lithiation. The peaks progressively move to higher potentials upon charging and lower potentials upon discharging in subsequent cycles. The area under each peak in 40 consecutive cycles gets successively smaller compared to those of the first two cycles, indicating a decreasing electrode activity and a rapid fade of the capacity. Compared to the LNO-OS electrode, the LNO-DS electrode delivers a more monotonous charge/discharge profile (Figure 3a), hinting at a quasi-solid-solution reaction during the Li-ion deintercalation and intercalation, as described below for the in situ SXRD results of LNO-DS electrode. During the first ten cycles, a subtle increase in the discharge capacity of the LNO-DS cathode (attaining a value of 198 mAh g^{-1} at the 10th cycle) is visible with increasing cycle number. Such a continuous activation process is often observed in surface-modified cathode materials.[41–43] Around 99% of the discharge capacity of the LNO-DS cathode is maintained for the subsequent 30 cycles (Figure 3e). Except for the first cycle, the dQ/dV curves of the selected cycles are almost completely overlapping (Figure 3c), which demonstrates the good cycling performance. Furthermore, the long-term cyclic stability of two cathodes was measured at 1 C for 100 cycles, as shown in Figure 3f. After 100 cycles, the discharge capacity of LNO-DS cathode is 178 mAh g^{-1}, retaining 89% of its initial capacity, which are higher than those of LNO-OS cathode (113 mAh g^{-1} and 53%).

To figure out the underlying mechanochemical mechanism, TXM-XANES was performed on the both electrodes in the discharged state after 40 cycles, as depicted in **Figure 4**. The morphology of the cycled particles is to a large extent maintained when compared with the apparent shape of pristine LNO-DS and LNO-OS particles, see Figure 4a,c and Figures S15 and S16 (Supporting Information). Macropores are obviously formed in the inner region of fatigued LNO-OS particles (see Figure 4d), whereas no hierarchical macroporous architecture is observed in the fatigued LNO-DS electrode (Figure 4b). The 3D rendering for the pores with diameters above the spatial resolution (21 nm) within a secondary particle of two cycled electrodes are shown in Figure 4e,f and Video S1 (Supporting Information). Excitingly, the area percentage of meso- and macropores of the cycled LNO-DS electrode is ≈0.3%, which is much smaller than that of the cycled LNO-OS electrode (≈1.7%), as shown in Figure S17 (Supporting Information). The generation of a

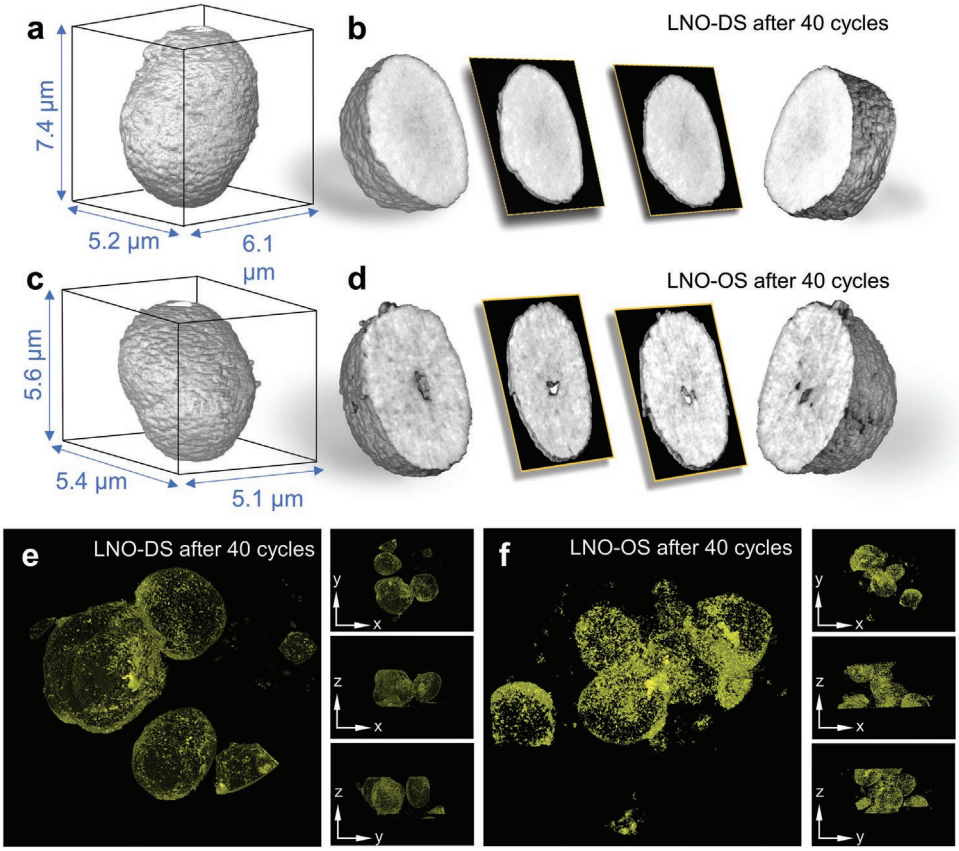

Figure 4. Mechanochemical degradation of two cathodes in the discharged state after over 40 cycles at 0.1 C. a) One secondary particle of fatigued LNO-DS electrode measured with 3D nano-tomography TXM, b) internal view and the corresponding cross-sectional view of the selected particle; c) rendering of one secondary particle of cycled LNO-OS electrode, d) internal view and the corresponding cross-sectional view of a fatigued particle, showing the formation of porous architecture inside LNO-OS crystallites caused by release of oxygen upon cycling; visualization of the pore size and their physical distribution within e) LNO-DS and f) LNO-OS cathodes after 40 cycles.

© 2022 The Authors. Advanced Functional Materials published by Wiley-VCH GmbH

16163028, 0, Downloaded from https://onlinelibrary.wiley.com/doi/10.1002/adfm.202211515 by Karlsruher Inst F. Technologie, Wiley Online Library on [18/12/2022]. See the Terms and Conditions (https://onlinelibrary.wiley.com/terms-and-conditions) on Wiley Online Library for rules of use; OA articles are governed by the applicable Creative Commons License

macroporous architecture in the fatigued LNO-OS cathode is supposed to result from the oxygen release during repeated Li-ion extraction/insertion.[44,45] These 3D macroporous architectures would expose the interior of the secondary agglomerates to the liquid electrolyte, promoting the formation of fresh active cathode electrolyte interphase (CEI) films on the primary particle surface, which, in turn, causes more side reactions to occur and strongly deteriorates the electrochemical performance of the LNO-OS electrode.[12,46] Although the formation of mesopores cannot be totally excluded since they are possibly smaller than the spatial resolution of the reconstructed image, the absence of macropores in cycled LNO-DS particles provides strong evidence that introducing a thin lattice-coherent surface protection layer could effectively mitigate oxygen release in LNO cathodes.

In-depth analysis of the Ni valence state of fatigued particles for LNO-DS and LNO-OS electrodes are shown in **Figure 5**. Color-coded mapping demonstrates that the Ni valence distribution in the cycled LNO-DS particles is relatively homogeneous (see Figure 5a–d) when compared with the cycled LNO-OS particles (Figure 5e–h). Representative few-pixel XANES spectra of fatigued LNO-DS and LNO-OS particles randomly selected from various regions are respectively depicted in Figure 5i,k. Only a small portion of Ni^{2+} (red color) is visible on the surface of the LNO-DS's secondary particles, the prevailing oxidation state of nickel is still 3+ in fatigued LNO-DS particles, proving a robust oxygen lattice structure framework and a stable 3D architecture of LNO-DS cathode over cycling. Importantly, there is no Ni^{2+} signal emerging from inside the selected particle of the fatigued LNO-DS electrode (Figure 5c,d). In contrast, TXM-XANES spectro-images of the cycled LNO-OS electrode reveal the presence of macropores inside the secondary particles. Evidently, the oxidation state of Ni ions in the near-surface area of primary particles is largely reduced to close to 2+ throughout the whole agglomerates (Figure 5g,h), whereas the inner region of primary crystallites still displays

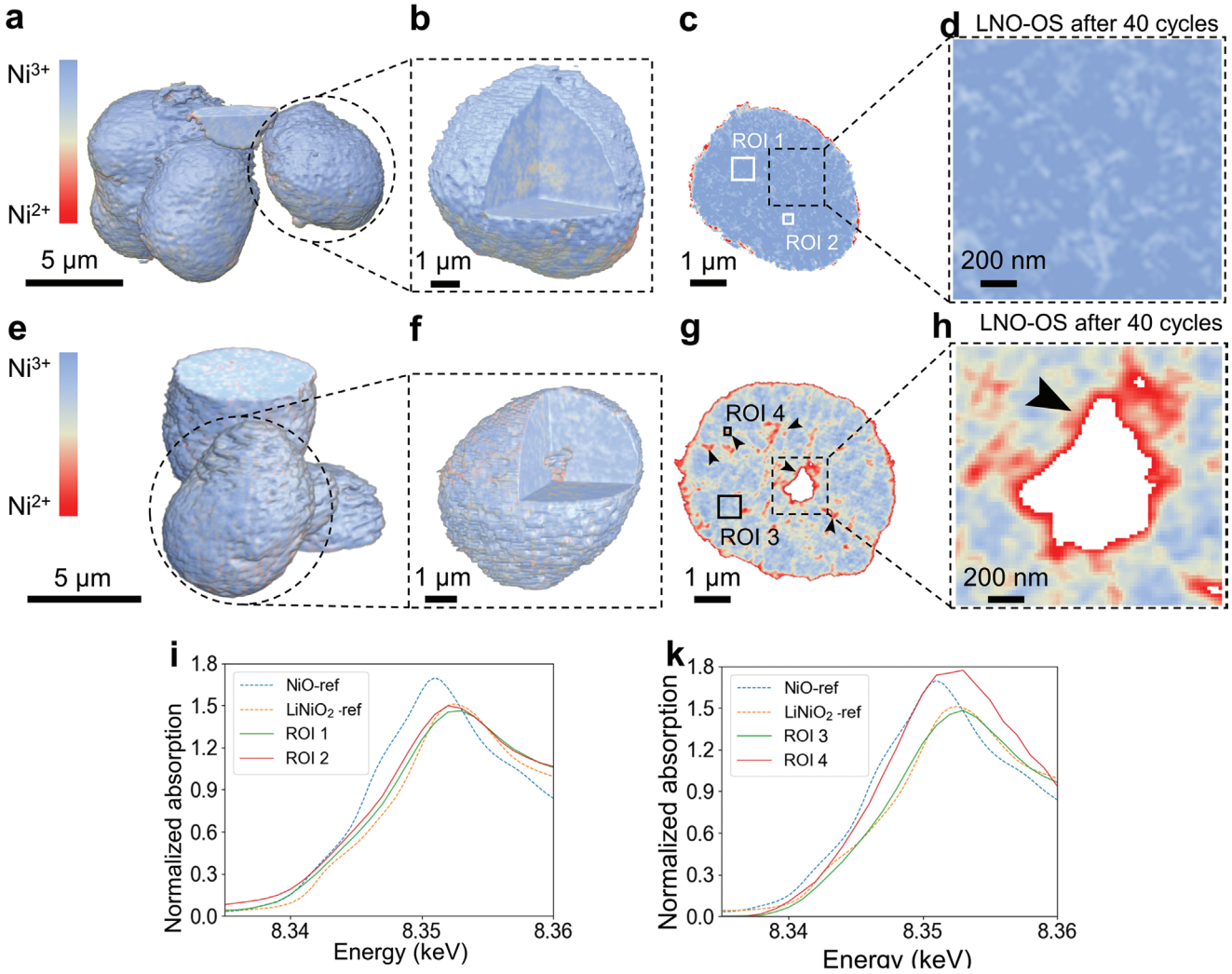

Figure 5. Spatial distribution of the Ni oxidation state in two cathodes after 40 cycles at 0.1 C (discharged state). a–d) Visualization of Ni's valence state distribution of fatigued LNO-DS particles and i) the corresponding Ni K-edge XANES spectra over ROIs in (c); e–h) visualization of Ni's valence state distribution and k) the corresponding Ni K-edge XANES spectra of fatigued LNO-OS particles over the ROIs in (g), providing unambiguous evidence for the surface inhomogeneity in the whole secondary spherical particles.

© 2022 The Authors. Advanced Functional Materials published by Wiley-VCH GmbH

16163028, 0, Downloaded from https://onlinelibrary.wiley.com/doi/10.1002/adfm.202211515 by Karlsruher Inst F. Technologie, Wiley Online Library on [18/12/2022]. See the Terms and Conditions (https://onlinelibrary.wiley.com/terms-and-conditions) on Wiley Online Library for rules of use; OA articles are governed by the applicable Creative Commons License

a Ni valence state of 3+ (light blue color). The reduction of Ni ions within the surface layer of the fatigued LNO-OS cathode further illustrates the oxygen release from the primary particle surface. Thence, an inferior cyclic property of LNO-OS cathode upon prolonged cycling is ascribed to the intrinsic chemomechanical degradation in secondary particles.

Considering that the phase transitions and oxygen release occurring during repeated lithiation/delithiation play a key role in the safety issue and electrochemical performance of LNO cathode materials, investigating the structural evolution of LNO-OS and LNO-DS electrodes is, therefore, fundamentally important. In situ SXRD experiments were carried out to further investigate the crystallographic changes of the two electrodes during cycling (2.8–4.3 V), the diffraction patterns of three selected angular regions along with the voltage as a function of reaction time are shown in **Figure 6**a,c. In order to clearly visualize and determine the phase transitions, the 3D maps of the evolution of the 003_h reflection are shown in Figure 6e,f. It is clear that the structural evolution of the two electrodes is quite different. There is a series of new reflections emerging in the LNO-OS electrode during the first charge/discharge cycle, reflecting a typical phase transition mechanism. The sequence of phase transitions observed during the first charging process (i.e., H1 → M → H2 → H3) is in good agreement with the three wide potential plateaus in the charge–voltage profile of the LNO-OS electrode (see Figure 3b). In contrast, the continuous variation of position and intensity of reflections upon cycling suggests a quasi-solid-solution reaction in the LNO-DS electrode, corresponding to the relatively short voltage plateaus and the broadening of dQ/dV peaks in Figure 3c. Besides, in situ XRD experiments[47] were also performed on both cathodes, see Figure 6b,d. The in situ XRD results of two electrodes collected at two different experimental setups were almost identical, manifesting that the SXRD analysis are accurate and reliable.

Each SXRD pattern of LNO-OS electrode acquired during the first cycle was fitted using Rietveld refinement with the rhombohedral structure model ($R\bar{3}m$) and/or the monoclinic structure model ($C2/m$). The resultant lattice parameters are represented in Figure 6g. In the initial stage of charge, all reflections in the SXRD patterns of the LNO-OS electrode could be assigned to a rhombohedral layered structure in hexagonal setting ($R\bar{3}m$, H1 phase). Upon the first charging, the pristine H1 phase remains unchanged until the state-of-charge (SoC) reaches up to ≈30%, see Figure 6c,f. As the delithiation of the LNO-OS electrode proceeds, a new monoclinic (M) layered phase starts to occur and grows at the expense of the H1 phase, as evidenced by a decreased intensity of the 101_h reflection and the appearance of new reflections $20\bar{1}_m$ and 110_m. Such a two-phase coexistence region in the LNO-OS electrode exists between the SoC of 30% and 45%. If there is no distortion, the monoclinic structure can be deduced from the hexagonal cell setting via the following transformation: $b_m = a_h = b_h$, $a_m = \sqrt{3}b_m$, and $c_m = 1/3 \times \sin\beta \times c_h$).[16,40] The single M phase is getting more distorted in the SoC region of 45–55% before it converts to the second H2 phase. It is worth mentioning that these phase transitions are accompanied by different Li/□ (□ for vacancy) ordering arrangement triggered by Jahn–Teller (JT) distortions,[16,48,49] as proposed by Arroyo y de Dompablo et al.[49] (see Figure S19, Supporting Information). Upon further de-lithiation, the remaining Li ions would rearrange and redistribute forming the Li/□ orderings in the layered structure, which could stabilize the Li-poor structure. Among these layered structures, the 180° Li_A–O–Ni–O–Li_B configurations are always retained with a JT active Ni^{3+} center. The JT effects are more pronounced when the charge is localized at the Ni^{3+} center, especially for the □–O–Ni–O–□ configurations. Thus, the distorted monoclinic structure is formed during charging because of the enhanced JT effect promoted by the increased number of Li vacancies. When SoC is above 60%, the remaining lithium ions are not capable of maintaining these special 180° configurations, leading to the generation of the H2 phase. As more Li ions are deintercalated from the layered structure (SoC > 80%), the unit cell displays a rapid contraction in the c direction, with the concomitant formation of the H3 phase. Since the LNO-DS electrode experiences a quasi-solid-solution reaction mechanism upon cycling, the SXRD patterns of LNO-DS electrode were fitted using a single rhombohedral layered structure model ($R\bar{3}m$). Lattice parameter changes of the LNO-DS electrode are comparable to those of the LNO-OS electrode. However, the c/a ratio of the H3 phase for the LNO-DS electrode is 4.81(3) and higher than that of the LNO-OS electrode of 4.73(3), evidencing a more stable layered structure in the LNO-DS electrode.[19,50,51] During the first lithiation, the changes of these lattice parameters for both electrodes take place in the reverse direction. The difference in unit-cell volume V of LNO-DS electrode before and after charging is –8.93(5) Å^3. The absolute change in unit volume of LNO-DS is smaller than –10.38(6) Å^3 for the LNO-OS electrode. After the electrodes were cycled at a current density of 1C for 100 cycles, a severe lattice distortion is clearly observed in the LNO-OS electrode, whereas the layered structure of LNO-OS electrode can be basically maintained (see Figure S20, Supporting Information). These results unambiguously confirm that the Li/Ni disordered layer on the surface of LNO-DS could effectively suppress the variation of unit-cell volume during cycling, providing a clear evidence that the lattice-coherent surface protection layer can stabilize the structural stability of the whole LNO-DS cathode.

To further confirm the enhanced structural stability of LNO with a disordered surface layer, the electrochemical properties of two electrodes were conducted within a voltage window of 2.8–4.7 V at 0.1 C (Figure S21, Supporting Information). It is clear that the discharge capacity of LNO-OS cathode declines faster than that of LNO-DS cathode. After 45 cycles, ≈79% of its first discharge capacity can be maintained for LNO-DS electrode, which is much higher than that of LNO-OS electrode (58%). In situ and ex situ SXRD results of two electrodes (Figures S22–S24, Supporting Information) during high-voltage cycling demonstrate that the structural collapse of LNO-OS cathode in the c direction at the SoC above 80% is more serious than that of LNO-DS cathode. These data indicate that the Li/Ni disordered layer on the surface of LNO primary particles could effectively mitigate structural fatigue even under the harsh operating condition of high voltage. The in situ SXRD analysis of two cathodes at different operating voltages, i.e., 2.8–4.3 V, and 2.8–4.7 V, unambiguously prove that the LNO-OS electrode suffers from a relatively large unit-cell volume change during cycling, which would trigger a successive loss of oxygen from surface lattice of primary particles.[15,52]

© 2022 The Authors. Advanced Functional Materials published by Wiley-VCH GmbH

16163028, 0, Downloaded from https://onlinelibrary.wiley.com/doi/10.1002/adfm.202211515 by Karlsruher Inst F. Technologie, Wiley Online Library on [18/12/2022]. See the Terms and Conditions (https://onlinelibrary.wiley.com/terms-and-conditions) on Wiley Online Library for rules of use; OA articles are governed by the applicable Creative Commons License

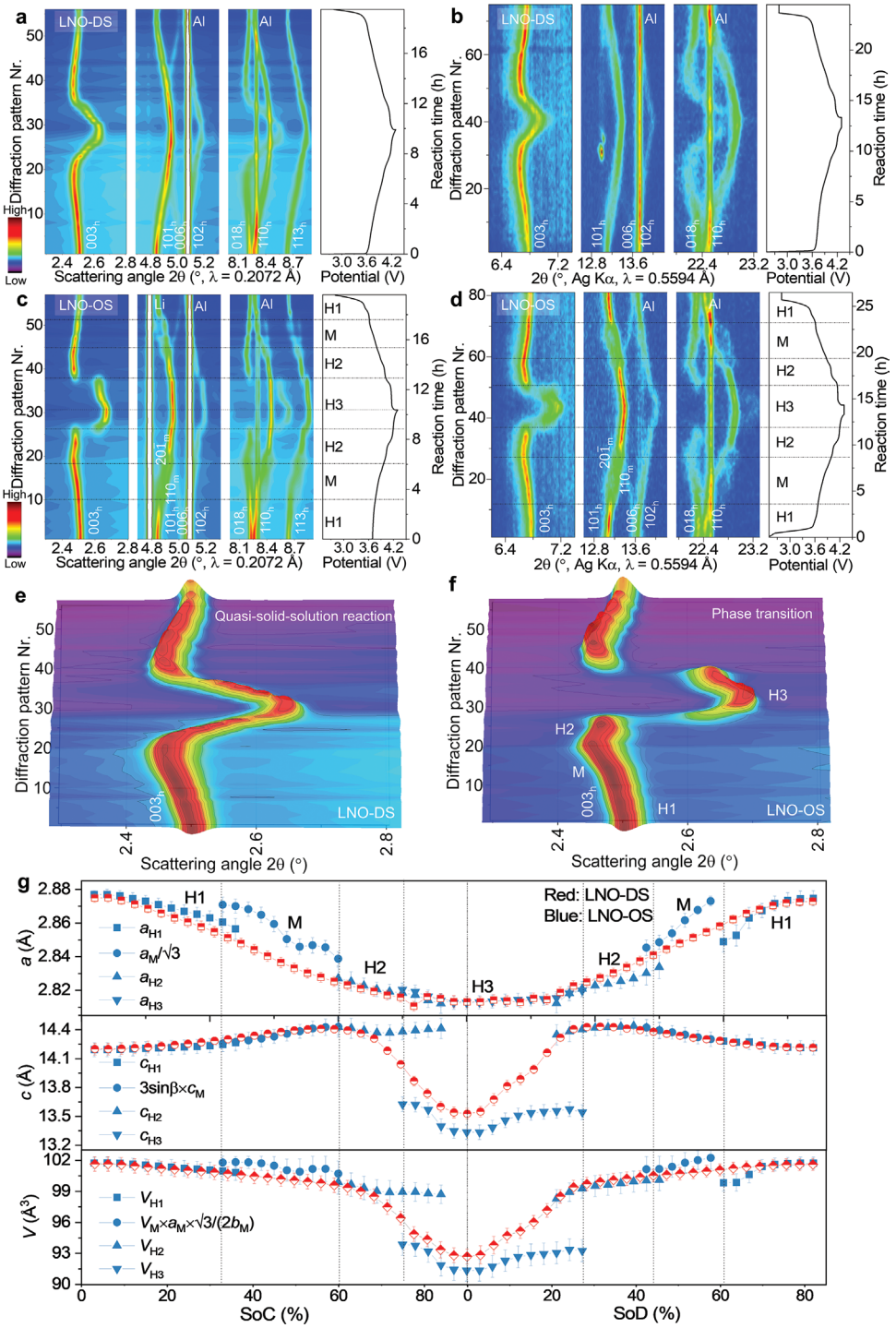

Figure 6. Crystallographic changes of both electrodes upon the Li^+ insertion/extraction process. Contour plot of in situ SXRD patterns of a) LNO-DS and c) LNO-OS electrodes during the first cycle between 2.8 and 4.3 V at 0.1 C, right figures show the corresponding charge-discharge voltage curves; the corresponding 3D maps of intensity and positions of the 003_h reflections for e) LNO-DS and f) LNO-OS electrodes, revealing that the (de)lithiation of these two electrodes occurs via different mechanisms. In situ XRD patterns (Ag Kα_1 radiation) of b) LNO-DS and d) LNO-OS cathodes during the 1st charge–discharge process between 2.7 and 4.3 V. g) The variation of lattice parameters of two cathodes, derived from the fitting of full SXRD patterns, as a function of SoC (state-of-charge) and SoD (state-of-discharge) during the first Li-ion extraction/insertion process.

Overall, the partially disordered layered $Li_{1-x}Ni_{1+x}O_2$ ($R\bar{3}m$) in the primary particle surface achieves the following targets. First, the ordered $LiNiO_2$ that takes up most of the particle volume contributes to high capacity due to its high reactivity of the Ni^{3+}/Ni^{4+} redox couple. Meanwhile, the epitaxially coherent Li-poor disordered phase near the surface contains Ni–O–Ni and Li–O–Ni configurations, and the 180° Ni–O–Ni super exchange chains prevent oxygen ions from escaping into the

© 2022 The Authors. Advanced Functional Materials published by Wiley-VCH GmbH

16163028, 0, Downloaded from https://onlinelibrary.wiley.com/doi/10.1002/adfm.202211515 by Karlsruher Inst F. Technologie, Wiley Online Library on [18/12/2022]. See the Terms and Conditions (https://onlinelibrary.wiley.com/terms-and-conditions) on Wiley Online Library for rules of use; OA articles are governed by the applicable Creative Commons License

electrolyte (see Figure S25, Supporting Information). Essentially, the partially disordered surface can be regarded "immunized" against oxygen loss upon electrochemical cycling, as evidenced by the absence of macroporous architecture within the fatigued LNO-DS particles and the mitigation of lattice distortion (see Figure 5a–d; Figure S20 and Video S1, Supporting Information). Second, the coherent disordered surface could efficiently preserve the mechanical integrity of the secondary particles since the oxygen cannot easily trespass the "immunized" disordered surface and flee into the electrolyte. Third, the detrimental H2 ⇌ H3 phase transition can be suppressed by the surface antisite defects because of an alleviated oxygen release at higher voltage regions (>4.1 V). As a consequence, the unit-cell volume change of LNO-DS cathode over cycling is relatively small (Figure 6; Figures S22 S23, Supporting Information), thereby, resulting in significantly improved cyclic stability. Accordingly, a necessary prerequisite for developing LNO cathode materials for EV applications is protecting the interior regions of secondary particles from electrolyte attack by suppressing generation of large pores (i.e., oxygen release).

3. Conclusion

In summary, synchrotron-based nano-resolution spectro-tomography techniques are employed to acquire in-depth understanding of the chemomechanical degradation and capacity fade in $LiNiO_2$ cathodes at the nano-to-micro-scales, providing 3D morphological and chemical information on the pristine and fatigued particles. A macroporous architecture is discovered in the LNO-OS electrode in the discharged state after 40 cycles at 0.1 C between 2.8 and 4.3 V. 3D full-field TXM XANES imaging demonstrates a reduction of Ni ions at the inner and outer surface of cycled LNO-OS particles because of the oxygen release upon the Li^+ insertion/extraction process. Such chemomechanical fatigue can be effectively mitigated through introducing Li/Ni antisite defects on the primary particle surface. Both the microstructure and the nickel oxidation state of LNO-DS are well retained after cycling because the coherent disordered surface layer is intrinsically stable in the lattice framework to mitigate the oxygen release. In situ SXRD results reveal that the LNO-DS electrode shows a quasi-solid-solution reaction during the process of Li-ion intercalation/deintercalation, in sharp contrast to the phase transition mechanism in the LNO-OS electrode. Moreover, small changes in the unit cell volume of the layered structure for the LNO-DS cathode upon cycling are also favorable for enhancing the structural and cyclic stability. As a consequence, the capacity retention of LNO-DS electrode is ≈89% after 100 cycles at 1 C, which is much higher than that of LNO-OS electrode (≈53%). Thereby, this work offers a viable approach for suppressing oxygen loss in order to accelerate the practical use of the high-energy $LiNiO_2$ and very Ni-rich cathodes with long-term stability.

Supporting Information

Supporting Information is available from the Wiley Online Library or from the author.

Acknowledgements

W.H. acknowledges the National Natural Science Foundation of China (grant no. 22108218), "Young Talent Support Plan" of Xi'an Jiaotong University (71211201010723) and Qinchuangyuan Innovative Talent Project (QCYRCXM-2022-137). This work was financially supported by the Guangxi Science and Technology Base and Talents Special Project (Grant No. AD21159007), the Natural Science Foundation of Guangxi (Grant No. 2020GXNSFBA297029). The authors acknowledge DESY (Hamburg, Germany), a member of the Helmholtz Association HGF, and BNL's National Synchrotron Light Source II (NSLS-II) for the provision of experimental facilities. Parts of this research were carried out at PETRA III beamlines P02.1 and P64. Beamtime was allocated for proposal(s) I-20220583, I-20220585, I-20210736, I-20210715, and I-20200642. Our research work has gained benefit from beamtime allocation at BL04-MSPD at ALBA Synchrotron (proposal number: 2020094655), Barcelona, Spain. The TEM characterization was supported by the Karlsruhe Nano Micro Facility (KNMF, http.www.knmf.kit.edu), a Helmholtz research infrastructure at Karlsruhe Institute of Technology (KIT, http.www.kit.edu). The authors acknowledge the help of Lucas Martin Brauch from KIT for STEM image simulations. The authors also thank the Instrument Analysis Center of Xi'an Jiao Tong University for the assistance test. This work contributes to the research performed at CELEST (Center for Electrochemical Energy Storage Ulm-Karlsruhe) and was supported by the German Research Foundation (DFG) under Project ID 390874152 (POLiS Cluster of Excellence).

Open access funding enabled and organized by Projekt DEAL.

Conflict of Interest

The authors declare no conflict of interest.

Author Contributions

J.C., Y.Y., and Y.T. contributed equally to this work. W.H. conceived the idea and discussed with H.L, S.W., M.K., H.E., and S.I.. W.H., Y.W., and L.H. carried out the preparation experiments; Y.T. performed the TEM experiments. Y.Y. and X.X. performed the synchrotron based TXM-XANES experiments. W.H., M.S.D.D., M.E., A.M., and A.T. performed the synchrotron based diffraction and absorption measurements. The data were analyzed by J.C., Y.Y. and W.H. and S.W.; J.C., Y.Y., S.W. and W.H. wrote the preliminary draft. All authors revised the manuscript and have given the approval to the final version of the manuscript.

Data Availability Statement

The data that support the findings of this study are available on request from the corresponding author. The data are not publicly available due to privacy or ethical restrictions.

Keywords

chemomechanical degradation, $LiNiO_2$ cathodes, oxygen release, self-protecting layers, tomography

Received: October 5, 2022
Revised: November 6, 2022
Published online:

© 2022 The Authors. Advanced Functional Materials published by Wiley-VCH GmbH

16163028, 0, Downloaded from https://onlinelibrary.wiley.com/doi/10.1002/adfm.202211515 by Karlsruher Inst F. Technologie, Wiley Online Library on [18/12/2022]. See the Terms and Conditions (https://onlinelibrary.wiley.com/terms-and-conditions) on Wiley Online Library for rules of use; OA articles are governed by the applicable Creative Commons License

[1] T. C. Liu, J. J. Liu, L. X. Li, L. Yu, J. C. Diao, T. Zhou, S. N. Li, A. Dai, W. G. Zhao, S. Y. Xu, Y. Ren, L. G. Wang, T. P. Wu, R. Qi, Y. G. Xiao, J. X. Zheng, W. Cha, R. Harder, I. Robinson, J. G. Wen, J. Lu, F. Pan, K. Amine, *Nature* **2022**, *606*, 305.
[2] J. Li, N. Sharma, Z. Jiang, Y. Yang, F. Monaco, Z. Xu, D. Hou, D. Ratner, P. Pianetta, P. Cloetens, F. Lin, K. Zhao, Y. Liu, *Science* **2022**, *376*, 517.
[3] W. Hua, X. Yang, N. P. M. Casati, L. Liu, S. Wang, V. Baran, M. Knapp, H. Ehrenberg, S. Indris, *eScience* **2022**, *2*, 183.
[4] Z. Chen, Y. Ren, E. Lee, C. Johnson, Y. Qin, K. Amine, *Adv. Energy Mater.* **2013**, *3*, 729.
[5] Y. G. Zou, H. Mao, X. H. Meng, Y. H. Du, H. Sheng, X. Yu, J. L. Shi, Y. G. Guo, *Angew. Chem., Int. Ed.* **2021**, *60*, 26535.
[6] K. Märker, P. J. Reeves, C. Xu, K. J. Griffith, C. P. Grey, *Chem. Mater.* **2019**, *31*, 2545.
[7] Y. K. Han, S. Heng, Y. Wang, Q. T. Qu, H. H. Zheng, *ACS Energy Lett.* **2020**, *5*, 2421.
[8] H. M. K. Sari, X. F. Li, *Adv. Energy Mater.* **2019**, *9*, 1901597.
[9] Z. Zhu, D. Yu, Y. Yang, C. Su, Y. Huang, Y. Dong, I. Waluyo, B. Wang, A. Hunt, X. Yao, J. Lee, W. Xue, J. Li, *Nat. Energy* **2019**, *4*, 1049.
[10] W. M. Seong, K. H. Cho, J. W. Park, H. Park, D. Eum, M. H. Lee, I. S. Kim, J. Lim, K. Kang, *Angew Chem Int. Ed.* **2020**, *59*, 18662.
[11] W. Yang, W. Xiang, Y. X. Chen, Z. G. Wu, W. B. Hua, L. Qiu, F. R. He, J. Zhang, B. H. Zhong, X. D. Guo, *ACS Appl. Mater. Interfaces* **2020**, *12*, 10240.
[12] W. Hua, Z. Wu, M. Chen, M. Knapp, X. Guo, S. Indris, J. R. Binder, N. N. Bramnik, B. Zhong, H. Guo, S. Chou, Y.-M. Kang, H. Ehrenberg, *J. Mater. Chem. A* **2017**, *5*, 25391.
[13] H.-H. Sun, A. Manthiram, *Chem. Mater.* **2017**, *29*, 8486.
[14] D.-W. Jun, C. S. Yoon, U.-H. Kim, Y.-K. Sun, *Chem. Mater.* **2017**, *29*, 5048.
[15] K. Y. Park, Y. Zhu, C. G. Torres-Castanedo, H. J. Jung, N. S. Luu, O. Kahvecioglu, Y. Yoo, J. T. Seo, J. R. Downing, H. D. Lim, M. J. Bedzyk, C. Wolverton, M. C. Hersam, *Adv. Mater.* **2022**, *34*, 2106402.
[16] H. Li, W. Hua, X. Liu-Théato, Q. Fu, M. Desmau, A. Missyul, M. Knapp, H. Ehrenberg, S. Indris, *Chem. Mater.* **2021**, *33*, 9546.
[17] J. Zheng, Y. Ye, T. Liu, Y. Xiao, C. Wang, F. Wang, F. Pan, *Acc. Chem. Res.* **2019**, *52*, 2201.
[18] P. G. Bruce, A. Lisowskaoleksiak, M. Y. Saidi, C. A. Vincent, *Solid State Ionics* **1992**, *57*, 353.
[19] L. Wang, X. Lei, T. Liu, A. Dai, D. Su, K. Amine, J. Lu, T. Wu, *Adv. Mater.* **2022**, 2200744.
[20] H. Zhu, Y. Tang, K. M. Wiaderek, O. J. Borkiewicz, Y. Ren, J. Zhang, J. Ren, L. Fan, C. C. Li, D. Li, X. L. Wang, Q. Liu, *Nano Lett.* **2021**, *21*, 9997.
[21] H. Yu, Y. Cao, L. Chen, Y. Hu, X. Duan, S. Dai, C. Li, H. Jiang, *Nat. Commun.* **2021**, *12*, 4564.
[22] H. Kim, M. G. Kim, H. Y. Jeong, H. Nam, J. Cho, *Nano Lett.* **2015**, *15*, 2111.
[23] T. Liu, L. Yu, J. Lu, T. Zhou, X. Huang, Z. Cai, A. Dai, J. Gim, Y. Ren, X. Xiao, M. V. Holt, Y. S. Chu, I. Arslan, J. Wen, K. Amine, *Nat. Commun.* **2021**, *12*, 6024.
[24] W. B. Hua, B. Schwarz, R. Azmi, M. Muller, M. S. D. Darma, M. Knapp, A. Senyshyn, M. Heere, A. Missyul, L. Simonelli, J. R. Binder, S. Indris, H. Ehrenberg, *Nano Energy* **2020**, *78*, 105231.
[25] X. Li, A. Gao, Z. Tang, F. Meng, T. Shang, S. Guo, J. Ding, Y. Luo, D. Xiao, X. Wang, D. Su, Q. Zhang, L. Gu, *Adv. Funct. Mater.* **2021**, *31*, 2010291.
[26] J. Zheng, T. Liu, Z. Hu, Y. Wei, X. Song, Y. Ren, W. Wang, M. Rao, Y. Lin, Z. Chen, J. Lu, C. Wang, K. Amine, F. Pan, *J. Am. Chem. Soc.* **2016**, *138*, 13326.
[27] D. Kong, J. Hu, Z. Chen, K. Song, C. Li, M. Weng, M. Li, R. Wang, T. Liu, J. Liu, M. Zhang, Y. Xiao, F. Pan, *Adv. Energy Mater.* **2019**, *9*, 1901756.
[28] S. Wang, W. Hua, A. Missyul, M. S. D. Darma, A. Tayal, S. Indris, H. Ehrenberg, L. Liu, M. Knapp, *Adv. Funct. Mater.* **2021**, *31*, 2009949.
[29] W. Hua, M. Chen, B. Schwarz, M. Knapp, M. Bruns, J. Barthel, X. Yang, F. Sigel, R. Azmi, A. Senyshyn, A. Missiul, L. Simonelli, M. Etter, S. Wang, X. Mu, A. Fiedler, J. R. Binder, X. Guo, S. Chou, B. Zhong, S. Indris, H. Ehrenberg, *Adv. Energy Mater.* **2019**, *9*, 1803094.
[30] Y. Yang, R. Xu, K. Zhang, S. J. Lee, L. Mu, P. Liu, C. K. Waters, S. Spence, Z. Xu, C. Wei, D. J. Kautz, Q. Yuan, Y. Dong, Y. S. Yu, X. Xiao, H. K. Lee, P. Pianetta, P. Cloetens, J. S. Lee, K. Zhao, F. Lin, Y. Liu, *Adv. Energy Mater.* **2019**, *9*, 1900674.
[31] G. Qian, J. Wang, H. Li, Z. F. Ma, P. Pianetta, L. Li, X. Yu, Y. Liu, *Natl. Sci. Rev.* **2022**, *9*, nwab146.
[32] F. Lin, Y. Liu, X. Yu, L. Cheng, A. Singer, O. G. Shpyrko, H. L. Xin, N. Tamura, C. Tian, T. C. Weng, X. Q. Yang, Y. S. Meng, D. Nordlund, W. Yang, M. M. Doeff, *Chem. Rev.* **2017**, *117*, 13123.
[33] S. Spence, W. K. Lee, F. Lin, X. Xiao, *Nanotechnology* **2021**, *32*, 442003.
[34] Z. Lin, B. Gilbert, Q. L. Liu, G. Q. Ren, F. Huang, *J. Am. Chem. Soc.* **2006**, *128*, 6126.
[35] A. Navrotsky, *Proc. Natl. Acad. Sci.* **2004**, *101*, 12096.
[36] H. Park, A. Mesnier, S. Lee, K. Jarvis, A. Manthiram, J. H. Warner, *Chem. Mater.* **2021**, *33*, 4638.
[37] S. Hwang, S. M. Kim, S. M. Bak, S. Y. Kim, B. W. Cho, K. Y. Chung, J. Y. Lee, E. A. Stach, W. Chang, *Chem. Mater.* **2015**, *27*, 3927.
[38] L. Su, E. Jo, A. Manthiram, *ACS Energy Lett.* **2022**, *7*, 2165.
[39] J. Kim, H. Cho, H. Y. Jeong, H. Ma, J. Lee, J. Hwang, M. Park, J. Cho, *Adv. Energy Mater.* **2017**, *7*, 1602559.
[40] T. Ohzuku, A. Ueda, M. Nagayama, *J. Electrochem. Soc.* **1993**, *140*, 1862.
[41] F. Wu, S. Fang, M. Kuenzel, A. Mullaliu, J.-K. Kim, X. Gao, T. Diemant, G.-T. Kim, S. Passerini, *Joule* **2021**, *5*, 2177.
[42] H. Kobayashi, G. H. Yuan, Y. Gambe, I. Honma, *ACS Appl. Energy Mater.* **2021**, *4*, 9866.
[43] W. Liu, X. F. Li, D. B. Xiong, Y. C. Hao, J. W. Li, H. R. Kou, B. Yan, D. J. Li, S. G. Lu, A. Koo, K. Adair, X. L. Sun, *Nano Energy* **2018**, *44*, 111.
[44] C. Xu, K. Marker, J. Lee, A. Mahadevegowda, P. J. Reeves, S. J. Day, M. F. Groh, S. P. Emge, C. Ducati, B. Layla Mehdi, C. C. Tang, C. P. Grey, *Nat. Mater.* **2021**, *20*, 84.
[45] P. Yan, J. Zheng, Z. K. Tang, A. Devaraj, G. Chen, K. Amine, J. G. Zhang, L. M. Liu, C. Wang, *Nat. Nanotechnol.* **2019**, *14*, 602.
[46] L. de Biasi, B. Schwarz, T. Brezesinski, P. Hartmann, J. Janek, H. Ehrenberg, *Adv. Mater.* **2019**, *31*, 1900985.
[47] Y. Ming, W. Xiang, L. Qiu, W. B. Hua, R. Li, Z. G. Wu, C. L. Xu, Y. C. Li, D. Wang, Y. X. Chen, B. H. Zhong, F. R. He, X. D. Guo, *ACS Appl. Mater. Interfaces* **2020**, *12*, 8146.
[48] M. Mock, M. Bianchini, F. Fauth, K. Albe, S. Sicolo, *J. Mater. Chem. A.* **2021**, *9*, 14928.
[49] M. E. A. Y. de Dompablo, G. Ceder, *J. Power Sources* **2003**, *119*, 654.
[50] J. Lai, J. Zhang, Z. Li, Y. Xiao, W. Hua, Z. Wu, Y. Chen, Y. Zhong, W. Xiang, X. Guo, *Chem. Commun.* **2020**, *56*, 4886.
[51] Y. J. Guo, C. H. Zhang, S. Xin, J. L. Shi, W. P. Wang, M. Fan, Y. X. Chang, W. H. He, E. H. Wang, Y. G. Zou, X. A. Yang, F. Q. Meng, Y. Y. Zhang, Z. Q. Lei, Y. X. Yin, Y. G. Guo, *Angew. Chem., Int. Ed.* **2022**, e202116865.
[52] M. Bianchini, M. Roca-Ayats, P. Hartmann, T. Brezesinski, J. Janek, *Angew. Chem., Int. Ed.* **2019**, *58*, 10434.

© 2022 The Authors. Advanced Functional Materials published by Wiley-VCH GmbH

16163028, 0, Downloaded from https://onlinelibrary.wiley.com/doi/10.1002/adfm.202211515 by Karlsruher Inst F. Technologie, Wiley Online Library on [18/12/2022]. See the Terms and Conditions (https://onlinelibrary.wiley.com/terms-and-conditions) on Wiley Online Library for rules of use; OA articles are governed by the applicable Creative Commons License